Chemistry Europe
European Chemical Societies Publishing

WILEY VCH

Excellence in Chemistry Research

Announcing our new flagship journal

- Gold Open Access
- Publishing charges waived
- Preprints welcome
- Edited by active scientists

Meet the Editors of *ChemistryEurope*

Luisa De Cola
Università degli Studi di Milano Statale, Italy

Ive Hermans
University of Wisconsin-Madison, USA

Ken Tanaka
Tokyo Institute of Technology, Japan

ChemPubSoc Europe

DOI: 10.1002/chem.201700150

CHEMISTRY A European Journal Full Paper

Conducting Materials |*Hot Paper*|

Enhanced Electrochemical Properties of Li_3VO_4 with Controlled Oxygen Vacancies as Li-Ion Battery Anode

Kan Wang,[a] Changkun Zhang,[a] Haoyu Fu,[a] Chaofeng Liu,[a] Zhuoyu Li,[a] Wenda Ma,[a] Xianmao Lu,*[a] and Guozhong Cao*[a, b]

Abstract: Li_3VO_4, as a promising intercalation-type anode material for lithium-ion batteries, features a desired discharge potential (ca. 0.5–1.0 V vs. Li/Li^+) and a good theoretical storage capacity (590 $mAh\,g^{-1}$ with three Li^+ inserted). However, the poor electrical conductivity of Li_3VO_4 hinders its practical application. In the present work, various amounts of oxygen vacancies were introduced in Li_3VO_4 through annealing in hydrogen to improve its conductivity. To elucidate the influence of oxygen vacancies on the electrochemical performances of Li_3VO_4, the surface energy of the resulting material was measured with an inverse gas chromatography method. It was found that Li_3VO_4 annealed in pure hydrogen at 400 °C for 15 min exhibited a much higher surface energy (60.7 $mJ\,m^{-2}$) than pristine Li_3VO_4 (50.6 $mJ\,m^{-2}$). The increased surface energy would lower the activation energy of phase transformation during the charge–discharge process, leading to improved electrochemical properties. As a result, the oxygen-deficient Li_3VO_4 achieved a significantly improved specific capacity of 495 $mAh\,g^{-1}$ at 0.1 Ag^{-1} (381 $mAh\,g^{-1}$ for pristine Li_3VO_4) and retains 165 $mAh\,g^{-1}$ when the current density increases to 8 Ag^{-1}.

Introduction

With high energy density and energy storage efficiency, lithium-ion batteries (LIBs) are one of the most important energy-storage technologies and have been widely used in portable electronics, electric vehicles, and large energy storage systems.[1–5] One of the main challenges in the electrochemical performances of LIBs is to ensure high specific capacity and a suitable working voltage window of the electrodes.[6,7] Therefore, understanding the working mechanism of the electrode materials has been a critical factor in designing LIBs. Of the two electrodes in a LIB, the anode has a lower electrochemical potential and plays a critical role in enhancing the energy density of the battery within the safety window of the electrolyte.[7,8] Typical anode materials can be grouped into three categories according to different reaction mechanisms: 1) conversion-reaction materials including transition metal oxides and metal sulfides,[9] 2) alloying materials such as Si and Ge,[10,11] and 3) intercalation materials such as graphite, Ti, or V-based oxides.[12,13] Intercalation anodes possess good reversibility and cycling stability, as the host material would largely retain its crystal structure.[14] Graphite as an intercalation material has been commonly used as the anode in commercial LIBs. However, the electrochemical behavior of natural graphite strongly depends on electrolytes, which may enter the interlayers of graphite to induce further expanded interlayer spacing and hence exfoliation of the graphite. As a result, irreversible capacity loss and battery degradation occur during long term discharge–charge processes.[15] Spinel $Li_4Ti_5O_{12}$ is a typical zero-strain-insertion anode material, which features a high lithium ion diffusion coefficient (2×10^{-8} $cm^2\,s^{-1}$) and excellent rate capability and reversibility.[16] However, its low theoretical capacity (175 $mAh\,g^{-1}$) and relatively high phase transformation potential (1.54 V vs. Li/Li^+) limit its applications.[17,18] Li_3VO_4 (LVO) has been considered as a promising intercalation anode material for LIBs due to its small volume change during lithiation/delithiation,[19] relatively high theoretical capacity (394 $mAh\,g^{-1}$ between 0.2 and 3.0 V vs. Li/Li^+), as well as desirable working potential (ca. 0.5–1.0 V vs. Li/Li^+). However, LVO has a low electrical conductivity ($<10^{-10}$ $S\,cm^{-1}$).[20] A general approach to enhance its surface electronic conductivity is to form composites with electronically conductive materials,[21–23] although the synthesis is always complicated and the volume energy density may be reduced. Another strategy to tune the electrical conductivity and electrochemical reactions of LVO is by introducing ionic defects.[24,25] Oxygen vacancies, for example, have been demonstrated to improve the specific capacity and rate performance of LVO.[26–28]

[a] K. Wang, Dr. C. Zhang, Dr. H. Fu, Dr. C. Liu, Z. Li, W. Ma, Prof. Dr. X. Lu, Prof. Dr. G. Cao
Beijing Institute of Nanoenergy and Nanosystems
Chinese Academy of Sciences
National Center for Nanoscience and Technology (NCNST)
Beijing, 100083 (P.R. China)
E-mail: luxianmao@binn.cas.cn

[b] Prof. Dr. G. Cao
Department of Materials Science and Engineering
University of Washington
Seattle, WA 98195-2120 (USA)
E-mail: gzcao@u.washington.edu

Supporting information for this article can be found under: http://dx.doi.org/10.1002/chem.201700150.

In this work, we introduced surface oxygen vacancies into LVO through annealing in hydrogen and studied the impact on the lithium ion intercalation properties. It was found that with the formation of surface oxygen vacancies, the surface energy of LVO increased dramatically. The increased surface energy would lower the activation energy of phase transformation during the charge–discharge process, leading to improved electrochemical properties of LVO. As expected, when LVO was annealed in hydrogen at 400 °C for 15 min, it delivered a high capacity of 495 mAh g^{-1} at 0.1 Ag^{-1} and maintained a reversible capacity of 165 mAh g^{-1} at 8 Ag^{-1}; a performance that is much enhanced over pristine LVO (381 mAh g^{-1} at 0.1 Ag^{-1} and 58 mAh g^{-1} at 8 Ag^{-1}).

Experimental Section

Material synthesis and characterization

LVO was prepared by a simple solution reaction method followed by heat treatment. First, stoichiometric amounts of V_2O_5 (0.152 g) and $LiOH{\cdot}H_2O$ (0.21 g) were, in turn, added to a mixture of 60 mL ethyl alcohol and 20 mL deionized water. The mixture was then sonicated for 20 min and stirred for 6 h. After freeze-drying for 12 h, the resulting white powder was calcined at 650 °C for 2 h in a muffle furnace. The calcined LVO was then ground and annealed at different temperatures to find the optimal annealing temperature (400 °C), at which the LVO was then annealed for 15 (LVO-15), 30 (LVO-30), and 60 min (LVO-60), respectively, under pure hydrogen flow at 80 sccm. Pure argon was used during the heating up and cooling periods.

The crystal structure of LVO samples was characterized by X-ray diffraction (XRD) on an X'Pert^3 diffractometer (PANalytical, Netherlands) with $Cu_{K\alpha}$ radiation ($\lambda = 1.54056$ Å) over the range of 10° to 75° (2θ) with a step size of 0.013°. The diffraction peak positions of the samples were calibrated with NaCl. The morphologies of the products were investigated with a field emission scanning electron microscope (FESEM, Hitachi SU8020, Japan). X-ray photoelectron spectra (XPS) were acquired by using an X-ray photo electron spectrometer (ESCALAB 250Xi, USA). The surface area was obtained by N_2 adsorption–desorption analyses (ASAP 2020 HD88, USA).

The surface energy of the samples was measured with an inverse gas chromatography (IGC) surface energy analyzer (SEA, Surface Measurement Systems Ltd., London, UK). IGC is a versatile, sensitive, and powerful technique capable of determining the surface parameters of samples. Before taking any measurements, the columns were pretreated at 180 °C for 1 h under a hydrogen flow. Hydrogen was used as the carrier gas with a flow rate of 25 mL min^{-1}. The column temperature was 25 °C when the experiments were carried out. The probes were defined to be *n*-hexane, *n*-heptane, *n*-octane, and *n*-nonane for dispersive surface energy. Methane was used as a dead time probe. The retention times (τ), averaged over two injections, were determined by the Conder and Young method. The fractional surface energy of all samples was 0.05. Dispersive surface energy was obtained by the Schultz method. The monopolar probes, dichloromethane and ethyl acetate, were also injected in order to obtain the acid-base surface energy. However, the analyzed materials had strong interactions with those probes; thus no elution was detected.[29]

Electrochemical characterization

Standard CR2032 coin-type cells were used for electrochemical tests and the cells were assembled in an argon-filled glovebox with both oxygen and water contents less than 1 ppm. Celgard 2400 polypropylene film was used as the separator. The electrolyte was a 1 M solution of $LiPF_6$ in a mixture of ethylene carbonate (EC) and dimethyl carbonate (DMC) (the weight ratio of EC/DMC is 1:1). Li foils were used as the counter and reference electrodes. The electrode slurry consisted of 75 wt.% of active material, 20 wt.% of acetylene black and 5 wt.% of sodium carboxymethyl cellulose (CMC). The homogeneous slurry was coated on a Cu foil and dried in vacuum oven at 120 °C for 12 h. Galvanostatic charge–discharge tests were conducted on a self-acting battery tester (LAND CT2001A, China). Cyclic voltammetry (CV) and electrochemical impedance spectroscopy (EIS) tests were performed on a Solartron potentiostat. All electrochemical measurements were carried out in a voltage range of 0.01–3.00 V vs. Li/Li^+ and the frequencies of the EIS ranged from 100 kHz to 0.01 Hz.

Results and Discussion

LVO samples were annealed at temperatures ranging from 200 °C and up, in hydrogen, for 15 minutes. It was found that at temperatures higher than 400 °C, an impurity phase, $LiVO_2$, started to appear as revealed by XRD (Figure S1 in Supporting Information). For samples annealed at 200, 300, and 400 °C, all electrochemical characterizations indicated that LVO annealed at 400 °C outperformed those annealed at 200 and 300 °C in terms of both kinetic properties and rate performance (Figure S2).[21] Therefore, an annealing temperature of 400 °C was selected for further investigation.

For samples annealed at 400 °C for different times, the XRD diffraction peaks matched well with the orthorhombic Li_3VO_4 phase (JCPDS No.38–1247) with space group $Pnm2_1$, indicating the samples are free of impurity phases after reduction by hydrogen (Figure 1 a). In addition, the sharp diffraction peaks demonstrate the high crystallinity of the samples. Based on the Scherrer equation, the crystallite grain sizes of all the samples were about 70 nm. Compared to pristine LVO, the diffraction peaks of the annealed samples shifted to lower angles (Figure 1 b), indicating that the LVO lattice expanded upon annealing in hydrogen. The lattice expansion was also confirmed from the increasing lattice constants with annealing time (Table 1).This result was expected because due to the reduction by hydrogen, longer annealing would introduce more V^{4+} ions which have a larger ionic radius that that of V^{5+} (0.72 vs. 0.68 Å). The HRTEM images of four samples are shown in Figure S3, and the observed lattice spacings are in accordance with that of LVO. However, oxygen vacancies are difficult to capture as the samples are easily decomposed under the electron beam. This phenomenon may imply that oxygen vacancies in the LVO lattice are high energy active sites that may easily induce phase transitions under some special conditions. HRTEM is the projection of the three-dimensional structure to a two-dimensional image, so randomly distributed sporadic oxygen vacancies would be easily shadowed by other structural information. To confirm the change in V^{4+}/V^{5+} ratio with annealing, XPS analysis was carried out. As shown in Figure S4,

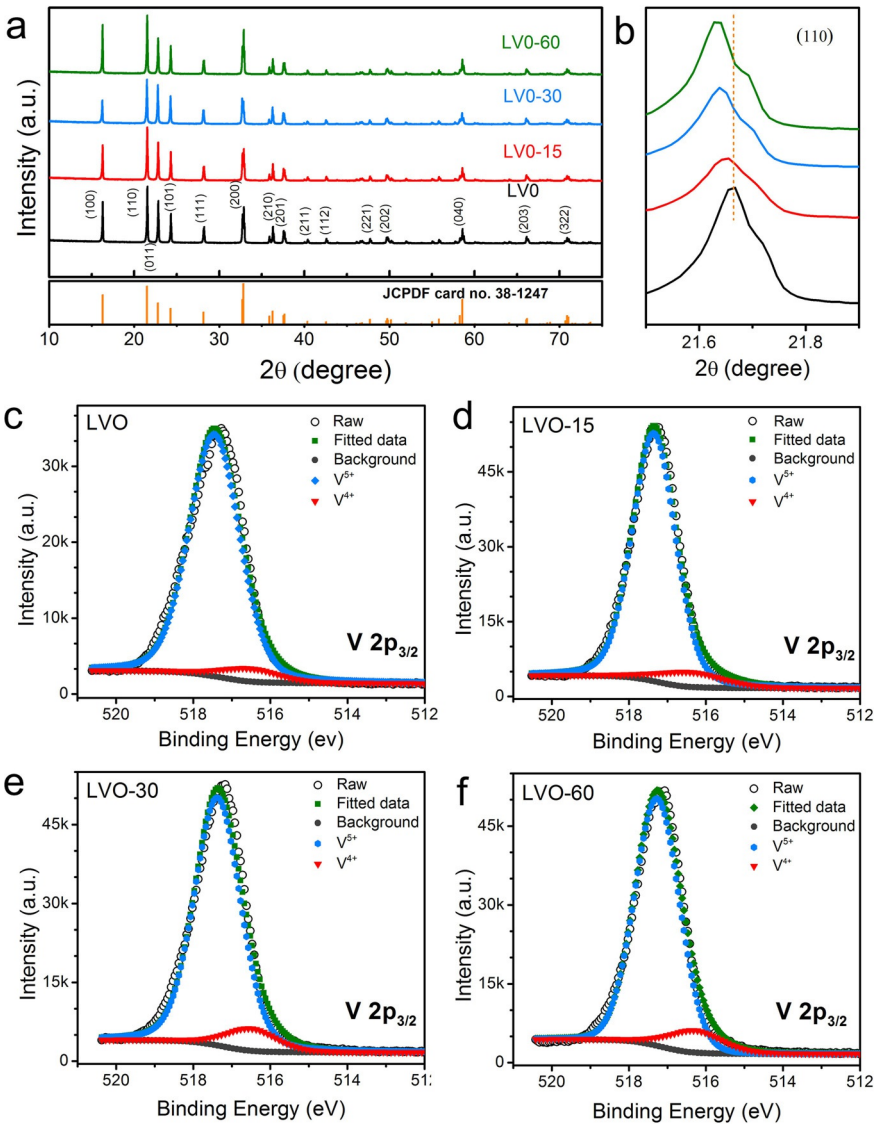

Figure 1. a) XRD patterns of the samples with different annealing times. b) Zoomed-in view of the (110) reflection. c–f) XPS spectra of V $2p_{3/2}$ for LVO, LVO-15, LVO-30, and LVO-60.

Table 1. Lattice parameters of the samples with different annealing times in hydrogen.

Sample	*a* [Å]	*b* [Å]	*c* [Å]
LVO	5.4234	6.2966	4.9295
LVO-15	5.4297	6.3030	4.9327
LVO-30	5.4311	6.3062	4.9340
LVO-60	5.4321	6.3082	4.9367

the V $2p_{3/2}$ binding energy shifted from 517.31 to 517.18 eV with increasing annealing time. The molar ratios of V^{4+}/V^{5+} of samples LVO, LVO-15, LVO-30, and LVO-60, estimated through peak deconvolution (Figure 1 c–f), were found to be 0.05, 0.08, 0.09, and 0.10, respectively, suggesting that longer hydrogen treatment lead to more V^{4+} ions at the surface of the samples. SEM images of the four samples suggest that both hydrogen treatment and annealing time show little influence on the morphology of LVO (Figure S5). In addition, BET tests reveal larger surface areas of hydrogen-treated samples compared with pristine LVO. In particular, LVO-15 possesses the highest BET surface area of 8.41 $m^2 g^{-1}$. The increased surface area of hydrogen-treated samples can be beneficial to the electrochemical performances.

A half-cell configuration was used to evaluate the electrochemical performance of the four samples. The voltage window was set between 0.01 and 3.00 V versus Li/Li^+. The cycling performance of the four samples is shown in Figure 2 a. At a current density of 1 Ag^{-1}, the discharge capacities of the first cycle were 357 mAh g^{-1} for LVO, 306 mAh g^{-1} for LVO-15, 296 mAh g^{-1} for LVO-30, and 257 mAh g^{-1} for LVO-60, respectively. Although the pristine LVO electrode displayed the highest capacity in the initial cycles, its capacity begins to decline sharply after 110 cycles and dropped to 159 mAh g^{-1} at the 500th cycle due to the low electrical conductivity of LVO.[14] The annealed samples, however, showed unusual cycle curves

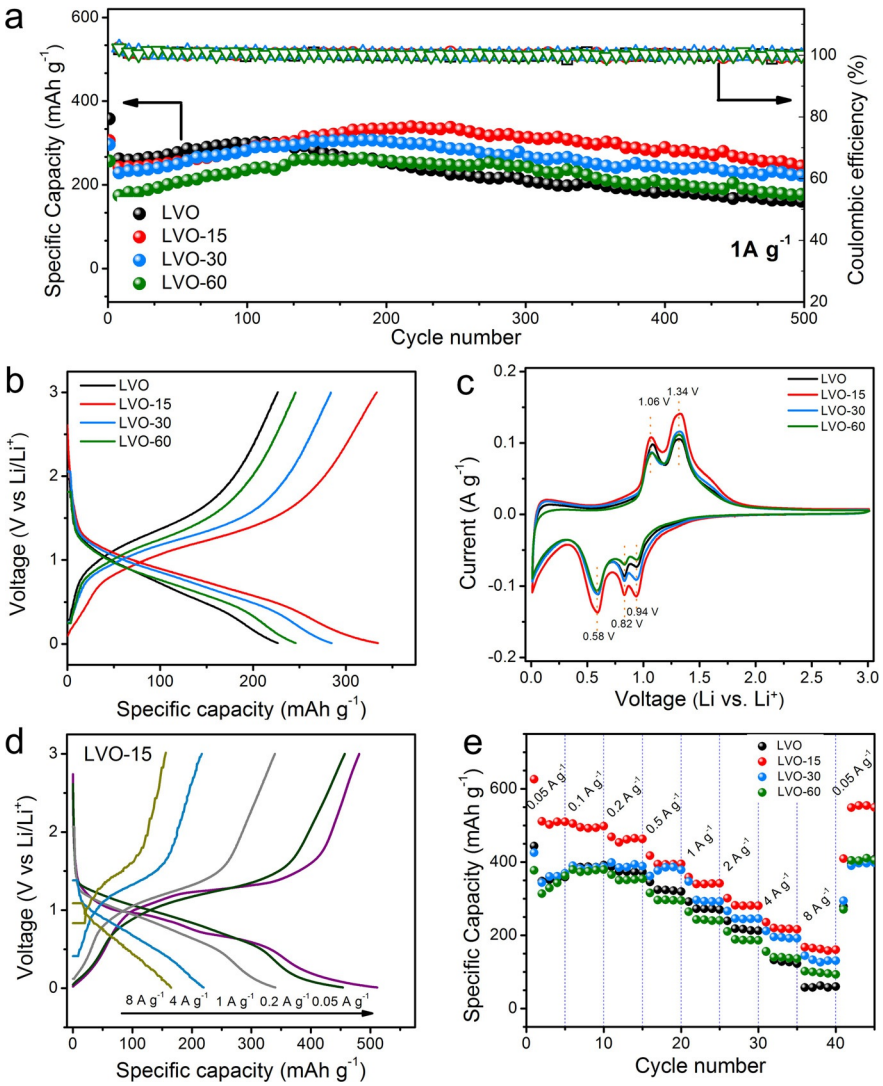

Figure 2. a) Charge–discharge cycling test of all samples at a current density of 1 Ag^{-1} for 500 cycles. b) Discharge and charge curves of all the sample electrodes for the 248th cycle at 1 Ag^{-1}. c) The second-cycle CV curves of the four samples at a voltage range of 0.01–3.00 V and a scan rate of 0.1 $mV s^{-1}$. d) The second charge–discharge curve of LVO-15 at various current densities of 0.05–8.00 Ag^{-1}. e) Discharge capacity of all the samples at different current densities in the voltage range of 0.01–3.00 V versus Li/Li^+.

compared with the pristine sample. LVO-15, for example, started with a lower initial capacity than pristine LVO, but it gradually increased until the 248th cycle, reaching a high capacity of 338 mAh g^{-1}. Although the discharge capacity decreased to 244 mAh g^{-1} after 500 cycles, it was still much higher than that of LVO (159 mAh g^{-1}). LVO-30 and LVO-60 electrodes exhibited similar discharge cycle curves, but the capacities decreased with annealing time, possibly attributed to the increased V^{4+}/V^{5+} ratio. Figure 2b shows the galvanostatic charge–discharge curves of the 248th cycle of the four samples, confirming that LVO-15 exhibited the highest capacity (338 mAh g^{-1}) of all four samples.

The long term cyclic curves for the hydrogen annealed samples exhibited a maximum capacity at around 248th cycle. The mechanism that led to such an activation of the electrode with increased cycle number is unclear, although similar results have been reported in the literature and some probable causes have been proposed.[26,30–32] For example, V_2O_5 xerogel electrodes annealed in N_2 exhibited an initial low discharge capacity of 68 mAh g^{-1} but increased in later cycles until reaching a high value of 158 mAh g^{-1}.[26] To explore the reason of this phenomenon, we compared the morphologies of LVO-15 before and after the cycling test (Figure S6 in Supporting Information). Before the charge–discharge test, LVO-15 showed a relatively smooth surface. After 500 cycles the LVO-15 electrode surface became rough and small particles appeared in the sample (Figure S6b). This result indicates that an electrochemical reconstruction process occurred during cycling test, causing the formation of smaller particles that offer better contact with electrolyte and promote the electrochemical reaction between the electrode and electrolyte.[33–35]

Cyclic voltammetric (CV) curves of all samples were measured at a scan rate of 0.1 $mV s^{-1}$ in the potential window of 3.00 to 0.01 V versus Li/Li^+ (Figures 2c, S7). For the first three

cycles, the CV curves of the four samples share similar profiles – the 1st cathodic scan showed two peaks at 0.75 and 0.52 V, corresponding to the formation of a solid-electrolyte interface (SEI);[33,36,37] but in the subsequent cycles, the two reduction peaks shifted to 0.85 and 0.53 V and a third peak located at 0.95 V emerged due to the activation of electrode materials.[38] The three reduction peaks at 0.53, 0.85, and 0.95 V can be ascribed to the phase transformation with the insertion of Li^+ ions into the electrodes. For all cycles, two oxidation peaks were observed at 1.06 and 1.34 V due to the extraction of Li^+ from $Li_{3+\gamma}VO_4$. Figure 2d shows the 2nd cycle charge–discharge curve of LVO-15 at different current densities. The discharge capacities of the LVO-15 electrode were 512, 495, 454, 393, 340, 282, 220, and 165 mAh g^{-1} at 0.05, 0.1, 0.2, 0.5, 1, 2, 4, and 8 Ag^{-1}, respectively. It is worth noting that at 8 Ag^{-1}, the pristine LVO electrode delivered a capacity of only one third of that of LVO-15 (58 vs. 165 mAh g^{-1}, Figure S8). The rate capabilities of the four electrodes are compared in Figure 2e, which shows that LVO-15 outperformed all the others at all current densities.

To understand the mechanism that causes the best electrochemical performance of LVO-15 among all samples, we measured the surface energies of the samples using an inverse gas chromatography (IGC) method.[29,39–41] The dispersive surface energy was determined by the *n*-hexane, *n*-heptane, *n*-octane and *n*-nonane probes. The retention of a gas probe molecule is defined as the amount of carrier gas required to elute the injected volume of probe molecules from the column, quantified by the net retention volume, V_n. During the test, the probe–probe interactions are negligible because the probes are infinitely diluted. Thus, V_n depends only on the interactions between the sample and probe molecules. The free energy of adsorption of the probe on the stationary phase surface per mole, ΔG_a, can be determined from V_n according to Equation (1):[42]

$$\Delta G_a = -RT\ln(V_n) + K \quad (1)$$

where R is the gas constant, T is the absolute column temperature, and K is a constant which depends on the chosen reference state. ΔG_a is also related to the work of adhesion (W_a) between the vapor probe and the solid stationary phase per unit of surface area as shown in Equation (2):

$$-\Delta G_a = NaW_a \quad (2)$$

where N is Avogadro's number and a is the surface area of an adsorbed probe molecule. If the probes are different *n*-alkane molecules and the dispersive interaction only occurs between the sample and probes, the work of adhesion can be presented as follows [Eq. (3)]:

$$W_a = W_a^b = 2\sqrt{\gamma_s^d}\sqrt{\gamma_l^d} \quad (3)$$

where γ_l^d and γ_s^d are the dispersive components of the surface energy of the liquid and the stationary phase, respectively. Then Equations (1)–(3) are combined to give Equation (4):[43]

$$RT\ln(V_n) = \sqrt{\gamma_s^d}2Na\sqrt{\gamma_l^d} + K \quad (4)$$

From Equation (4), it can be seen that $RT\ln(V_n)$ is proportional to $a\sqrt{\gamma_l^d}$ so that a series of nonpolar *n*-alkanes used as

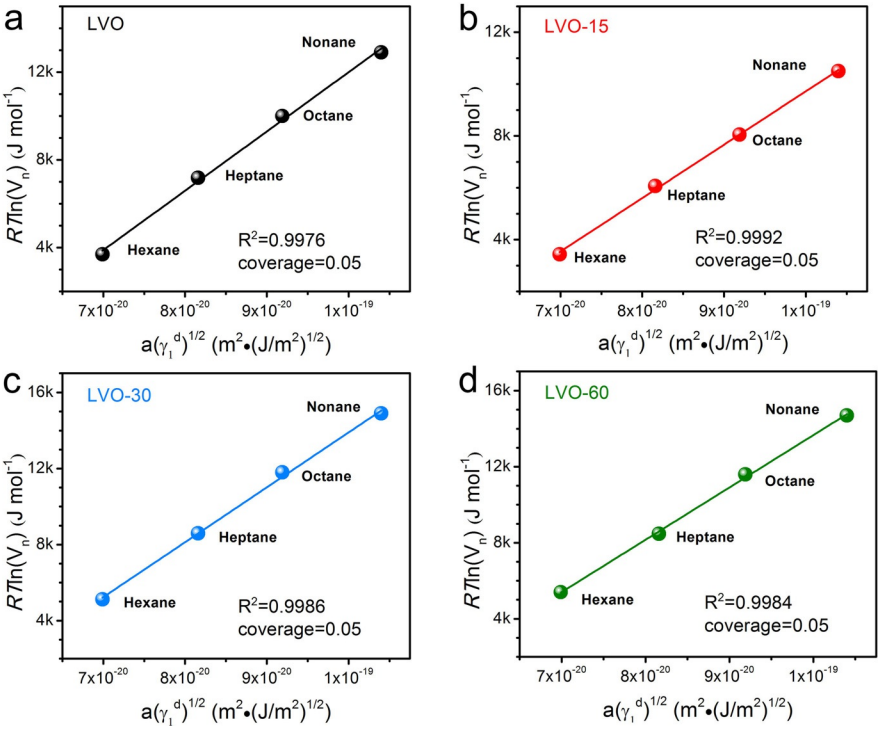

Figure 3. Plots of $RT\ln(V_n)$ versus $a\sqrt{\gamma_l^d}$ for the calculation of the dispersive part of surface energy for the samples.

probes can plot a line with $RT\ln(V_n)$ versus $a\sqrt{\gamma_l^d}$. The dispersive component of surface energy can be calculated by the slope of the fitted line.

Figure 3 shows that the plots of $RT\ln(V_n)$ against $a\sqrt{\gamma_l^d}$ of the four samples annealed with different times. According to the linear fit, the dispersive surface energies for LVO, LVO-15, LVO-30, and LVO-60 are 50.64, 60.67, 57.10, and 58.44 mJ m^{-2}. Clearly, all annealed samples exhibited a higher dispersive surface energy than that of pristine LVO, with the sample that was annealed for 15 min in hydrogen, LVO-15, showing the highest. The enhanced dispersive surface energy compared with pristine LVO can be attributed to more oxygen vacancies that induce more defects and active lattice sites due to annealing. With the introduction of oxygen vacancies, the defects derived from the oxygen vacancies may serve as nucleation centers with higher lattice energy. Therefore, less external energy is required to overcome the nucleation barrier and phase transition becomes much easier for reversible insertion and extraction of Li ions.[44,45] Therefore, the annealed samples exhibited much improved rate performance especially at high current densities.

The electrochemical impedance spectra (EIS) of the four samples are shown in Figure 4a. The EIS spectra consist of two parts: a compressed semicircle between the 100 kHz and 100 Hz shows the charge transfer resistance and constant-phase element of the electrodes, and a sloping line with an angle about 45° following the semicircle in the region of low frequencies reflects the diffusion of Li ions in the electrode bulk. An equivalent circuit, as shown in the inset of Figure 4a, was used to evaluate the values of the charge transfer resistance R_{ct} of the four samples (Table 2). Obviously, the smaller charge transfer resistances of the annealed samples LVO-15, LVO-30, and LVO-60 due to oxygen deficiency makes them more favorable for high rate performance than pristine LVO.

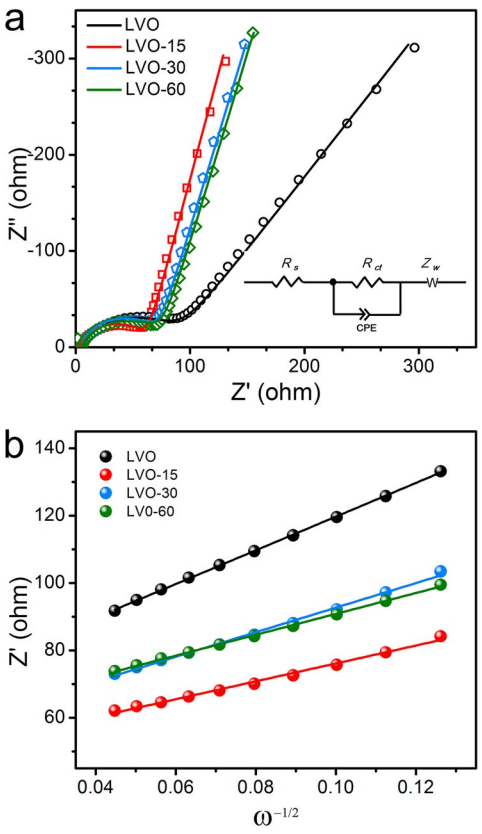

Figure 4. a) Nyquist plots of the electrodes before cycling tests. Inset shows the equivalent circuit where R_{ct} is the charge transfer resistance, R_s is the resistance of the electrolyte, *CPE* is the double layer capacitance, and Z_W is the Warburg resistance. b) Z′ versus $\omega^{-1/2}$ in the low frequency range.

Table 2. The charge transfer resistance, linear relation of Z' versus $\omega^{-1/2}$, and lithium diffusion coefficients of the four samples.

Sample	R_{ct}[a] [Ω]	X: $\omega^{-1/2}$; Y/Z'[b]	D_{Li}[c] [cm^2 s^{-1}]
LVO	79	$Y=500.27x+69.69$	7.11×10^{-17}
LVO-15	58	$Y=265.86x+49.55$	2.53×10^{-16}
LVO-30	67	$Y=364.78x+56.22$	1.34×10^{-16}
LVO-60	69	$Y=310.02x+59.85$	1.85×10^{-16}

[a] Charge transfer resistance. [b] Linear relation of Z' and $\omega^{-1/2}$. [c] Lithium diffusion coefficient.

In addition, the lithium diffusion coefficient (D_{Li}) can be calculated using Equation (5):

$$D = R^2T^2/2A^2n^4F^4C_0^2\sigma^2 \quad (5)$$

where R is the gas constant, T is the absolute temperature, F is the Faraday constant, n is the number of electrons transferred per molecule, A is the active surface area of the electrode (0.50 cm^2), C_0 is the concentration of lithium ions in the cathode (9.8×10^{-3} mol cm^{-3}), D is the apparent ion diffusion coefficient, and σ is the Warburg factor, which is relative to Z' and can be obtained from the slope of the lines in Figure 4b [Eq. (6)]:

$$Z' = R_D + R_L + \sigma\omega^{-1/2} \quad (6)$$

where R_D is ohmic solution resistance, and R_L is charge transfer resistance. The resulting lithium D_{Li} of the four samples are shown in Table 2. Compared to pristine LVO, the annealed electrodes exhibited much higher lithium diffusion coefficients. The above results clearly indicate that LVO annealed in hydrogen atmosphere presents a smaller charge-transfer resistance and higher lithium diffusion coefficient, offering much enhanced electrochemical performance.

Conclusions

Different amounts of oxygen vacancies in LVO were introduced by annealing in pure hydrogen at 400 °C for a various period of time. The oxygen-deficient samples showed improved rate performance and enhanced cyclic performance compared with pristine LVO. Specifically, LVO-15 (annealed for 15 min) demonstrated the highest discharge capacity of 495 mAh g^{-1} at 0.1 Ag^{-1}. At 8 Ag^{-1}, LVO-15 delivered a capacity of 165 mAh g^{-1}, nearly three times higher than that of pristine

LVO (58 mAh g^{-1}). The improved lithium ion storage performance of oxygen-deficient samples could be attributed to the introduction of oxygen vacancies, which might have served as nucleation or catalysis centers to facilitate fast phase transformation during the lithium ion intercalation/de-intercalation process.

Acknowledgements

This work was supported by the "Thousand Talents" program for pioneering researchers and their innovation team, China.

Conflict of interest

The authors declare no conflict of interest.

Keywords: conducting materials · hydrogen annealing · Li_3VO_4 · lithium-ion batteries · oxygen vacancies · surface energy

[1] H. D. Yoo, E. Markevich, G. Salitra, D. Sharon, D. Aurbach, *Mater. Today* **2014**, *17*, 110 – 121.
[2] S. S. Zhang, *J. Power Sources* **2006**, *161*, 1385 – 1391.
[3] R. C. Massé, E. Uchaker, G. Cao, *Sci. China Mater.* **2015**, *58*, 715 – 766.
[4] Z. Yang, J. Zhang, M. C. W. Kintner-Meyer, X. Lu, D. Choi, J. P. Lemmon, J. Liu, *Chem. Rev.* **2011**, *111*, 3577 – 3613.
[5] Q. Zhang, E. Uchaker, S. L. Candelaria, G. Cao, *Chem. Soc. Rev.* **2013**, *42*, 3127 – 3171.
[6] J. B. Goodenough, *Energy Storage Materials* **2015**, *1*, 158 – 161.
[7] C. Liu, R. Massé, X. Nan, G. Cao, *Energy Storage Materials* **2016**, *4*, 15 – 58.
[8] J. B. Goodenough, Y. Kim, *Chem. Mater.* **2010**, *22*, 587 – 603.
[9] R. Malini, U. Uma, T. Sheela, M. Ganesan, N. G. Renganathan, *Ionics* **2009**, *15*, 301 – 307.
[10] N. Liu, Z. Lu, J. Zhao, M. T. McDowell, H. W. Lee, W. Zhao, Y. Cui, *Nat. Nanotechnol.* **2014**, *9*, 187 – 192.
[11] Y. Zhao, X. F. Li, B. Yan, D. B. Xiong, D. J. Li, S. Lawes, X. L. Sun, *Adv. Energy Mater.* **2016**, *6*, 1502175.
[12] D. McNulty, D. N. Buckley, C. O'Dwyer, *J. Power Sources* **2014**, *267*, 831 – 873.
[13] L. F. Shen, E. Uchaker, X. G. Zhang, G. Z. Cao, *Adv. Mater.* **2012**, *24*, 6502 – 6506.
[14] H. Li, X. Liu, T. Zhai, D. Li, H. Zhou, *Adv. Energy Mater.* **2013**, *3*, 428 – 432.
[15] M. Winter, G. H. Wrodnigg, J. O. Besenhard, W. Biberacher, P. Novák, *J. Electrochem. Soc.* **2000**, *147*, 2427.
[16] K. Zaghib, M. Simoneau, M. Armand, M. Gauthier, *J. Power Sources* **1999**, *81 – 82*, 300 – 305.
[17] G.-N. Zhu, H.-J. Liu, J.-H. Zhuang, C.-X. Wang, Y.-G. Wang, Y.-Y. Xia, *Energy Environ. Sci.* **2011**, *4*, 4016 – 4022.
[18] T. Ohzuku, A. Ueda, N. Yamamoto, *J. Electrochem. Soc.* **1995**, *142*, 1431 – 1435.
[19] S. Ni, X. Lv, J. Ma, X. Yang, L. Zhang, *J. Power Sources* **2014**, *248*, 122 – 129.
[20] E. Iwama, N. Kawabata, N. Nishio, K. Kisu, J. Miyamoto, W. Naoi, P. Rozier, P. Simon, K. Naoi, *ACS Nano* **2016**, *10*, 5398 – 5404.
[21] C. Zhang, C. Liu, X. Nan, H. Song, Y. Liu, C. Zhang, G. Cao, *ACS Appl. Mater. Interfaces* **2016**, *8*, 680 – 688.
[22] X. Liu, S. Shi, Q. Xiong, L. Li, Y. Zhang, H. Tang, C. Gu, X. Wang, J. Tu, *ACS Appl. Mater. Interfaces* **2013**, *5*, 8790 – 8795.
[23] Q. Li, J. Sheng, Q. Wei, Q. An, X. Wei, P. Zhang, L. Mai, *Nanoscale* **2014**, *6*, 11072 – 11077.
[24] C. Liu, Z. G. Neale, G. Cao, *Mater. Today* **2016**, *19*, 109 – 123.
[25] E. Uchaker, G. Cao, *Chem. Asian J.* **2015**, *10*, 1608 – 1617.
[26] D. Liu, Y. Liu, B. B. Garcia, Q. Zhang, A. Pan, Y.-H. Jeong, G. Cao, *J. Mater. Chem.* **2009**, *19*, 8789.
[27] N. Li, K. Du, G. Liu, Y. Xie, G. Zhou, J. Zhu, F. Li, H.-M. Cheng, *J. Mater. Chem. A* **2013**, *1*, 1536 – 1539.
[28] J. Chen, Z. Ding, C. Wang, H. Hou, Y. Zhang, C. Wang, G. Zou, X. Ji, *ACS Appl. Mater. Interfaces* **2016**, *8*, 9142 – 9151.
[29] C. Zhang, K. Wang, C. Liu, X. Nan, H. Fu, W. Ma, Z. Li, G. Cao, *NPG Asia Materials* **2016**, *8*, e287.
[30] J. Cho, T.-J. Kim, B. Park, *J. Electrochem. Soc.* **2002**, *149*, A288.
[31] B. Kang, G. Ceder, *Nature* **2009**, *458*, 190 – 193.
[32] J. Liu, P.-J. Lu, S. Liang, J. Liu, W. Wang, M. Lei, S. Tang, Q. Yang, *Nano Energy* **2015**, *12*, 709 – 724.
[33] S. Ni, X. Lv, J. Zhang, J. Ma, X. Yang, L. Zhang, *Electrochim. Acta* **2014**, *145*, 327 – 334.
[34] C. Wang, D. Wang, Q. Wang, H. Chen, *J. Power Sources* **2010**, *195*, 7432 – 7437.
[35] S. Ni, X. Lv, T. Li, X. Yang, L. Zhang, Y. Ren, *Electrochim. Acta* **2013**, *96*, 253 – 260.
[36] S. Ni, J. Zhang, J. Ma, X. Yang, L. Zhang, *J. Power Sources* **2015**, *296*, 377 – 382.
[37] Z. Jian, M. Zheng, Y. Liang, X. Zhang, S. Gheytani, Y. Lan, Y. Shi, Y. Yao, *Chem. Commun.* **2015**, *51*, 229 – 231.
[38] M. Sevilla, R. Mokaya, *Energy Environ. Sci.* **2014**, *7*, 1250.
[39] U. V. Shah, Z. Wang, D. Olusanmi, A. S. Narang, M. A. Hussain, M. J. Tobyn, J. Y. Y. Heng, *Int. J. Pharm.* **2015**, *495*, 234 – 240.
[40] J. A. F. Gamelas, E. Ferraz, F. Rocha, *Colloids Surf. A* **2014**, *455*, 49 – 57.
[41] W. Ma, C. Zhang, C. Liu, X. Nan, H. Fu, G. Cao, *ACS Appl. Mater. Interfaces* **2016**, *8*, 19542 – 19549.
[42] P. Mukhopadhyay, H. P. Schreiber, *Colloids Surf. A* **1995**, *100*, 47 – 71.
[43] S. Mohammadi-Jam, K. E. Waters, *Adv. Colloid Interface Sci.* **2014**, *212*, 21 – 44.
[44] A. Stabel, K. Eichhorst-Gerner, J. P. Rabe, A. R. González-Elipe, *Langmuir* **1998**, *14*, 7324 – 7326.
[45] H. Song, C. Liu, C. Zhang, G. Cao, *Nano Energy* **2016**, *22*, 1 – 10.

Manuscript received: January 11, 2017
Accepted Article published: February 28, 2017
Final Article published: March 27, 2017